Interferometry by deconvolution, Part 1— Theory for acoustic waves and numerical examples

Ivan Vasconcelos[1] and Roel Snieder[2]

ABSTRACT

Interferometry allows for synthesis of data recorded at any two receivers into waves that propagate between these receivers as if one of them behaves as a source. This is accomplished typically by crosscorrelations. Based on perturbation theory and representation theorems, we show that interferometry also can be done by deconvolutions for arbitrary media and multidimensional experiments. This is important for interferometry applications in which (1) excitation is a complicated source-time function and/or (2) when wavefield separation methods are used along with interferometry to retrieve specific arrivals. Unlike using crosscorrelations, this method yields only causal scattered waves that propagate between the receivers. We offer a physical interpretation of deconvolution interferometry based on scattering theory. Here we show that deconvolution interferometry in acoustic media imposes an extra boundary condition, which we refer to as the free-point or clamped-point boundary condition, depending on the measured field quantity. This boundary condition generates so-called free-point scattering interactions, which are described in detail. The extra boundary condition and its associated artifacts can be circumvented by separating the reference waves from scattered wavefields prior to interferometry. Three wavefield-separation methods that can be used in interferometry are direct-wave interferometry, dual-field interferometry, and shot-domain separation. Each has different objectives and requirements.

INTRODUCTION

The main objective of seismic interferometry is to obtain the impulse response between receivers without any knowledge about model parameters (Weaver and Lobkis, 2001; Wapenaar et al., 2004;

Weaver and Lobkis, 2004). Typically, interferometry is implemented by crosscorrelating recorded data (Curtis et al., 2006; Larose et al., 2006). Many of the formal proofs and arguments surrounding interferometry are based on crosscorrelations. Proofs based on correlation representation theorems state the validity of interferometry for acoustic waves (Lobkis and Weaver, 2001; Weaver and Lobkis, 2004), for elastic media (Wapenaar et al., 2004; Draganov et al., 2006), and for attenuative (Snieder, 2007) and perturbed media (Vasconcelos, 2007). Other proofs of interferometry based on time reversal is offered by Fink (2006) and by Bakulin and Calvert (2006) in their virtual-source methodology. Schuster et al. (2004) and Yu and Schuster (2006) use correlation-based interferometry embedded within an asymptotic migration scheme for interferometric imaging. Snieder (2004), Sabra et al. (2004), Roux et al. (2004), Snieder et al. (2006a), and Snieder et al. (2006b) rely on the stationary-phase method to explain results from interferometry.

Interferometry has been applied in ultrasonics (Weaver and Lobkis, 2001; Malcolm et al., 2004; van Wijk, 2006), helioseismology (Rickett and Claerbout, 1999), global seismology (Sabra et al., 2005a; Shapiro et al., 2005), and ocean acoustics (Roux et al., 2004; Sabra et al., 2005b). Curtis et al. (2006) and Larose et al. (2006) give comprehensive interdisciplinary reviews of interferometry. As the understanding of interferometry progresses, new applications of the method become feasible. For example, reservoir engineering might benefit from interferometry; Snieder (2006) shows that principles of interferometry also hold for the diffusion equation. In an even more general framework, interferometry can be applied to a wide class of partial differential equations, which include the Schrödinger and advection equations (Wapenaar et al., 2006; Snieder et al., 2007).

The goal in this paper is to gain insight into interferometry from yet another point of view. Although interferometry is done typically by correlations, it is natural to wonder if it could be accomplished by deconvolutions. This issue is raised by Curtis et al. (2006) as one of the standing questions within interferometry. We claim that interferometry can indeed be accomplished by deconvolutions for arbitrary, multidimensional media. Deconvolution interferometry has the ad-

vantage of being independent of source properties. Successful examples of deconvolution interferometry have been reported: Trampert et al. (1993) use deconvolution to extract the SH-wave propagator matrix and to estimate attenuation, Snieder and Şafak (2006) recover the elastic response of a building using deconvolutions, and Mehta et al. (2007b, c) obtained the near-surface propagator matrix using deconvolutions from the recording of a teleseismic event in a borehole seismometer array.

In a paper that spawned much of today's work on interferometry, Riley and Claerbout (1976) suggested the use of deconvolution to retrieve the earth's 1D reflectivity response. They then turned to correlation because it tends to be more stable. Loewenthal and Robinson (2000) show that the deconvolution of dual wavefields can be used to change the boundary conditions of the original experiment to generate only upgoing scattered waves at the receiver locations and to recover reflectivity. In a series of papers on free-surface multiple suppression, Amundsen and coworkers use inverse deconvolution operators designed to remove the free-surface boundary condition (e.g., Amundsen et al., 2001; Holvik and Amundsen, 2005). The topics of multiple suppression and interferometry are related intrinsically because of the ability to manipulate boundary conditions (Riley and Claerbout, 1976; Wapenaar et al., 2004; Berkhout and Verschuur, 2006; Snieder et al., 2006b; Mehta et al., 2007a). Consequently, previous work on deconvolution-based multiple suppression also is related to the practice of interferometry.

Using a combination of perturbation theory and representation theorems (as in Vasconcelos, 2007), we first review interferometry by correlations. In our discussion on correlation-based interferometry, we restrict ourselves to key aspects that help define deconvolution interferometry. Following, we give a derivation in which we represent deconvolution interferometry by a series similar in form to the Lippmann-Schwinger scattering series (Rodberg and Thaler, 1967; Weglein et al., 2003). We first analyze the meaning of leading-order terms in the scattered wavefield and discuss the role of higher-order terms of the deconvolution interferometry series in Appendix A. Next, we compare our deconvolution-based method with crosscorrelation interferometry. We discuss the role played by different wavefield-separation methods in seismic interferometry and, in particular, how these approaches benefit deconvolution interferometry. Finally, using a single-layer model, we illustrate the main concepts of deconvolution interferometry while comparing it to its correlation-based counterpart. In Vasconcelos and Snieder (2008; hereafter called Part 2), we provide results of deconvolution interferometry for complex models that are consistent with the discussion presented here.

Although our intent is not to discuss a specific use for interferometry by deconvolution, we point out that this method will be of most use for interferometry applications that (1) require the suppression of the source function or (2) involve some sort of wavefield-separation procedure. In Part 2, we present a specific application of deconvolution interferometry, providing both numerical and field-data examples of drill-bit seismic imaging. Broadside imaging of the San Andreas fault at Parkfield, California (Vasconcelos et al., 2007), was successful because of deconvolution interferometry (see Part 2). Apart from drill-bit seismics, complicated source signals can be generated by other types of man-made noise (e.g., traffic noise, running engines) or by natural noise sources such as seismic and microseismic events coming from the subsurface, ocean waves, or thunderbolts during a thunderstorm.

In examples by Trampert et al. (1993), Snieder and Şafak (2006), and Mehta et al. (2007b, c), deconvolution is used to eliminate the earthquake signal, which contains arrivals of different modes and/or multiple scattered waves. In the method by Loewenthal and Robinson (2000), deconvolution collapses all downgoing waves into a spike at zero time, leaving only the upgoing earth response. These are but a few examples of applications within exploration geophysics in which deconvolution interferometry plays an important role.

THEORY OF INTERFEROMETRY

Review of interferometry by crosscorrelations

Let frequency-domain wavefield $u(\mathbf{r}_A, \mathbf{s}, \omega)$ recorded at $\mathbf{r}_A$ be the superposition of the unperturbed and scattered Green's functions $G_0(\mathbf{r}_A, \mathbf{s}, \omega)$ and $G_S(\mathbf{r}_A, \mathbf{s}, \omega)$, respectively, convolved with a source function $W(\mathbf{s}, \omega)$ associated with an excitation at $\mathbf{s}$; hence,

$$u(\mathbf{r}_A, \mathbf{s}, \omega) = W(\mathbf{s}, \omega)[G_0(\mathbf{r}_A, \mathbf{s}, \omega) + G_S(\mathbf{r}_A, \mathbf{s}, \omega)]. \quad (1)$$

Although here, and throughout the text, we call G_S the scattered wavefield, G_S formally represents a wavefield perturbation. In our derivations, we rely on perturbation theory (Weglein et al., 2003; Vasconcelos, 2007), such that the quantities G_0 and $G = G_0 + G_S$ represent background and perturbed wavefields, respectively, that satisfy the equation for acoustic (Vasconcelos, 2007), elastic (Wapenaar et al., 2004), and possibly attenuative waves (Snieder, 2007). The quantities G_0 and G_S can represent generally unperturbed waves and wavefield perturbations, respectively.

For simplicity, we refer to G_0 and G_S in the context of classical scattering theory (e.g., Rodberg and Thaler, 1967), where G_0 is a direct wave and G_S contains all scattered waves. However, our discussion is not restricted to the classical scattering problem. Throughout this paper, we treat only acoustic waves. Both the background medium and medium perturbation can be arbitrarily heterogeneous and anisotropic. In addition, $W(\mathbf{s}, \omega)$ can be a complicated function of frequency and can vary as a function of $\mathbf{s}$.

The crosscorrelation of wavefields measured at $\mathbf{r}_A$ and $\mathbf{r}_B$ (equation 1) gives, in the frequency domain,

$$C_{AB} = |W(\mathbf{s})|^2 G(\mathbf{r}_A, \mathbf{s}) G^*(\mathbf{r}_B, \mathbf{s}); \quad (2)$$

where the asterisk denotes complex conjugation. From equation 2, it follows that the crosscorrelation C_{AB} depends on the power spectrum of $W(\mathbf{s})$. Note that we omit the frequency dependence of equation 2 for brevity; we do the same for all subsequent equations.

Next, we integrate the crosscorrelations in equation 2 over a surface $\partial\mathbb{V}$ (Appendix A) that includes all sources $\mathbf{s}$, giving

$$\oint_{\partial\mathbb{V}} C_{AB} d\mathbf{s} = \langle |W(\mathbf{s})|^2 \rangle [G(\mathbf{r}_A, \mathbf{r}_B) + G^*(\mathbf{r}_A, \mathbf{r}_B)], \quad (3)$$

where $\langle |W(\mathbf{s})|^2 \rangle$ is the source average of the power spectra (Snieder et al., 2007) and where $G(\mathbf{r}_A, \mathbf{r}_B)$ and $G^*(\mathbf{r}_A, \mathbf{r}_B)$ are the causal and anticausal Green's functions, respectively, for an excitation at $\mathbf{r}_B$ and receiver at $\mathbf{r}_A$. For equation 3 to hold, G corresponds to the pressure response in acoustic media (e.g., Wapenaar and Fokkema, 2006). If G is the particle-velocity response, the plus sign on the right-hand side of equation 3 is replaced by a minus sign (e.g., Wapenaar and Fokkema, 2006). Equation 3 is valid strictly for lossless media. Snieder (2007) shows how interferometry can be accomplished in attenuative acoustic media.

The average of the power spectrum of source $\langle |W(\mathbf{s})|^2 \rangle$ can be a complicated function of frequency (or time); hence, recovering the response between receivers at $\mathbf{r}_A$ and $\mathbf{r}_B$ through equation 3 can be difficult. Most authors suggest deconvolving $\langle |W(\mathbf{s})|^2 \rangle$ after the integration in equation 3 (Wapenaar et al., 2004; Fink, 2006; Snieder et al., 2006a; Snieder et al., 2006b). This assumes an independent estimate of the power spectrum of the source is available. Indeed, in some applications, such an estimate can be obtained (Mehta et al., 2007a); often, however, independent estimates of the power spectrum of the source are not available. Part 2 deals with specific drill-bit seismic examples for which independent estimates of source function are not available, and correlation-based interferometry (equation 3) does not provide acceptable results. In the next two sections, we provide alternative interferometry methodologies that recover the impulse response between receivers without requiring independent estimates of the power spectrum of the source function.

For the moment, we assume a source function independent of source position $\mathbf{s}$ ($W(\mathbf{s}) = W$) in equations 1–3. By combining equations 1 and 2, we can expand C_{AB} into four terms:

$$
\begin{aligned}
C_{AB} &= u(\mathbf{r}_A, \mathbf{s})u^*(\mathbf{r}_B, \mathbf{s}) \\
&= \underbrace{u_0(\mathbf{r}_A, \mathbf{s})u_0^*(\mathbf{r}_B, \mathbf{s})}_{C_{AB}^1} + \underbrace{u_S(\mathbf{r}_A, \mathbf{s})u_0^*(\mathbf{r}_B, \mathbf{s})}_{C_{AB}^2} \\
&\quad + \underbrace{u_0(\mathbf{r}_A, \mathbf{s})u_S^*(\mathbf{r}_B, \mathbf{s})}_{C_{AB}^3} + \underbrace{u_S(\mathbf{r}_A, \mathbf{s})u_S^*(\mathbf{r}_B, \mathbf{s})}_{C_{AB}^4}
\end{aligned}
$$

$$(4)$$

where $u_0 = WG_0$ and $u_S = WG_S$ (see equation 1). The four terms, C_{AB}^1 through C_{AB}^4, can be inserted into equation 3, giving

$$
\begin{aligned}
\oint_{\partial\mathbb{V}} C_{AB}^1 d\mathbf{s} &+ \oint_{\partial\mathbb{V}} C_{AB}^2 d\mathbf{s} + \oint_{\partial\mathbb{V}} C_{AB}^3 d\mathbf{s} + \oint_{\partial\mathbb{V}} C_{AB}^4 d\mathbf{s} \\
&= |W|^2 \big[G_0(\mathbf{r}_A, \mathbf{r}_B) + G_S(\mathbf{r}_A, \mathbf{r}_B) \\
&\quad + G_0^*(\mathbf{r}_A, \mathbf{r}_B) + G_S^*(\mathbf{r}_A, \mathbf{r}_B) \big].
\end{aligned}
$$

$$(5)$$

Each of the four integrals on the left-hand side of equation 5 has a different physical meaning. Using representation theorems, Vasconcelos (2007) analyzes how each integral in equation 5 relates to terms in the right-hand side of the equation. For imaging purposes, we only want to use the G_S terms (scattered waves) in equation 5. The first integral relates to unperturbed terms on the right-hand side of equation 5 to give

$$
\oint_{\partial\mathbb{V}} u_0(\mathbf{r}_A, \mathbf{s})u_0^*(\mathbf{r}_B, \mathbf{s}) d\mathbf{s} = |W|^2 \big[G_0(\mathbf{r}_A, \mathbf{r}_B) + G_0^*(\mathbf{r}_A, \mathbf{r}_B) \big].
$$

$$(6)$$

The relationship in equation 6 is not surprising because unperturbed wavefields u_0 satisfy the unperturbed wave equation. Consequently, interferometry of unperturbed wavefields on the left-hand side of equation 6 must yield the causal and anticausal unperturbed wavefields between $\mathbf{r}_B$ and $\mathbf{r}_A$ (right side of equation 6). A less obvious relationship between the terms in equation 5 is that, as described in Appendix A, the dominant contribution to the causal scattered wavefield between $\mathbf{r}_B$ and $\mathbf{r}_A$ comes from the correlation between the unperturbed wavefield at $\mathbf{r}_B$ and scattered wavefield at $\mathbf{r}_A$:

$$
\int_{\partial\mathbb{V}_1} u_S(\mathbf{r}_A, \mathbf{s})u_0^*(\mathbf{r}_B, \mathbf{s}) d\mathbf{s} \approx |W|^2 G_S(\mathbf{r}_A, \mathbf{r}_B),
$$

$$(7)$$

where $\partial\mathbb{V}_1$ is a portion of $\partial\mathbb{V}$ that yields stationary-phase contributions to $G_S(\mathbf{r}_A, \mathbf{r}_B)$ (Appendix A). Based on Appendix A, we argue that this relationship holds for most types of experiments in exploration seismology (surface seismic, many vertical seismic profiling experiments, etc.).

Equation 7 is an approximate relationship because it neglects the influence of a volume integral that corrects for medium perturbations located on the stationary paths of unperturbed waves that propagate from sources $\mathbf{s}$ to a receiver at $\mathbf{r}_B$ (Appendix A; see also Part 2). In the context of seismic imaging, the extraction of $G_S(\mathbf{r}_A, \mathbf{r}_B)$ is the objective of interferometry.

An important requirement for the successful application of interferometry is that waves must be propagating at all directions at each receiver location. This condition is referred to as *equipartioning* (Weaver and Lobkis, 2004; Larose et al., 2006; Sánchez-Sesma and Campillo, 2006; Snieder et al., 2007). Other authors (Wapenaar et al., 2004; Draganov et al., 2006) mention the necessity of having many sources distributed closely around a closed-surface integral, such as in equation 3. However, in exploration experiments, it is impossible to surround the subsurface with sources. Consequently, we end up with only a partial source integration instead of the closed-surface integration necessary for equation 3 to hold.

As pointed out by Snieder et al. (2006a) and Snieder et al. (2006b) truncation of the surface integral can introduce spurious events in the final interferometric gathers. This holds for general 3D models as well, and it can be verified because

$$
\begin{aligned}
\int_{\partial\mathbb{V}_1} C_{AB}\, d\mathbf{s} &+ \int_{\partial\mathbb{V}_2} C_{AB}\, d\mathbf{s} \\
&= |W|^2 \big[G(\mathbf{r}_A, \mathbf{r}_B) + G^*(\mathbf{r}_A, \mathbf{r}_B) \big],
\end{aligned}
$$

$$(8)$$

where $\partial\mathbb{V}_1$ and $\partial\mathbb{V}_2$ are surface segments such that $\partial\mathbb{V}_1 \cup \partial\mathbb{V}_2 = \partial\mathbb{V}$. Suppose that in an actual field experiment we could acquire only data with waves excited over the surface $\partial\mathbb{V}_1$ (such as in equation 7). Then, as we can see from equation 8, the integration over all available sources (the integral over $\partial\mathbb{V}_1$) would result in the desired response (right-hand side of equation 8) minus the integral over $\partial\mathbb{V}_2$. In this case, if the integral over $\partial\mathbb{V}_2$ were nonzero (i.e., stationary contributions are associated with sources placed over $\partial\mathbb{V}_2$), then data synthesized from interferometry over $\partial\mathbb{V}_1$ would contain spurious events associated with the missing sources on $\partial\mathbb{V}_2$.

Although this may appear to be a practical limitation of interferometry, the lack of primary sources in the subsurface is, in practice, somewhat compensated by multiple scattering or by reflections below the region of interest (Wapenaar, 2006; Halliday et al., 2007). In field experiments, some of the desired system equipartioning can be achieved with longer recording times, making up for some of the missing sources over $\partial\mathbb{V}_2$. For long recording times, equipartioning can arise in multiple scattering regimes that produce waves carrying similar amounts of energy propagating in all directions. Because this is a model-dependent problem, it is difficult, in practice, to predetermine the influence of missing sources and to what extent longer recording times make up for the absence of these sources.

Deconvolution interferometry

As we have seen, the crosscorrelation of wavefields $u(\mathbf{r}_A,\mathbf{s})$ and $u(\mathbf{r}_B,\mathbf{s})$ contains the power spectrum of the excitation function (equation 2). Instead, deconvolution of $u(\mathbf{r}_A,\mathbf{s})$ with $u(\mathbf{r}_B,\mathbf{s})$ gives

$$D_{AB} = \frac{u(\mathbf{r}_A,\mathbf{s})}{u(\mathbf{r}_B,\mathbf{s})} = \frac{u(\mathbf{r}_A,\mathbf{s})u^*(\mathbf{r}_A,\mathbf{s})}{|u(\mathbf{r}_B,\mathbf{s})|^2} = \frac{G(\mathbf{r}_A,\mathbf{s})G^*(\mathbf{r}_B,\mathbf{s})}{|G(\mathbf{r}_B,\mathbf{s})|^2}.$$

(9)

Now the source function $W(\mathbf{s})$ (equation 1) is canceled by the deconvolution process. Although no multidimensional deconvolution interferometry approach has been presented to date, it is intuitive to proceed with the integration

$$\oint_{\partial\mathbb{V}} D_{AB}\, d\mathbf{s} = \oint_{\partial\mathbb{V}} \frac{G(\mathbf{r}_A,\mathbf{s})G^*(\mathbf{r}_B,\mathbf{s})}{|G(\mathbf{r}_B,\mathbf{s})|^2} d\mathbf{s} \qquad (10)$$

to mimic interferometry by crosscorrelation (equation 3).

The existing proofs for the validity of interferometry by crosscorrelation (equation 3) are not immediately applicable to interferometry by deconvolution. For example, representation theorems (e.g., Wapenaar et al., 2004; Wapenaar et al., 2006; Vasconcelos, 2007) are not applicable to the spectral ratio of wavefields. In addition, stationary-phase evaluation of the integral in equation 10 for a specified model (such as used by Snieder et al., 2006a) is compromised by the presence of $|G(\mathbf{r}_B,\mathbf{s})|^2$ in the denominator. Despite being zero phase, $|G(\mathbf{r}_B,\mathbf{s})|^2$ contains cross terms between unperturbed and scattered wavefields (see below), which make the denominator in equation 10 an oscillatory function that prevents the stationary-phase method (Bleistein and Handelsman, 1975) from being applied directly to equation 10.

Our solution to evaluating the integral in equation 10 is to expand the denominator in a power series, which then allows us to give a physical interpretation to deconvolution interferometry. We begin by making the expansion

$$\frac{1}{G(\mathbf{r}_B,\mathbf{s})} = \frac{1}{G_0(\mathbf{r}_B,\mathbf{s}) + G_S(\mathbf{r}_B,\mathbf{s})}$$

$$= \frac{1}{G_0(\mathbf{r}_B,\mathbf{s})\big(1 + G_S(\mathbf{r}_B,\mathbf{s})/G_0(\mathbf{r}_B,\mathbf{s})\big)}$$

$$= \frac{1}{G_0(\mathbf{r}_B,\mathbf{s})}\left(1 + \sum_{n=1}^{\infty} (-1)^n \left(\frac{G_S(\mathbf{r}_B,\mathbf{s})}{G_0(\mathbf{r}_B,\mathbf{s})}\right)^n\right),$$

(11)

which is valid for small perturbations, i.e., when $|G_S|^2 \ll |G_0|^2$. After inserting equation 11 into equation 9, we get

$$D_{AB} = \frac{G(\mathbf{r}_A,\mathbf{s})}{G_0(\mathbf{r}_B,\mathbf{s})} + \frac{G(\mathbf{r}_A,\mathbf{s})G_0^*(\mathbf{r}_B,\mathbf{s})}{|G_0(\mathbf{r}_B,\mathbf{s})|^2}$$

$$\times \sum_{n=1}^{\infty} (-1)^n \left(\frac{G_S(\mathbf{r}_B,\mathbf{s})}{G_0(\mathbf{r}_B,\mathbf{s})}\right)^n.$$

(12)

From now on we refer to equation 12 as the deconvolution interferometry series. This representation of equation 9 is more convenient to describe the physics of deconvolution interferometry, as we discuss in the next sections.

Contributions to first order in the scattered wavefield

We focus our discussion on terms that dominate contributions to the deconvolution interferometry integral in equation 10. These terms are of interest in geophysical applications such as interferometric imaging (Wapenaar, 2006). After inserting equation 12 into the integral in equation 10 and keeping only terms that are linear in the wavefield perturbations G_S, we get

$$\oint_{\partial\mathbb{V}} D_{AB}\, d\mathbf{s} = \underbrace{\oint_{\partial\mathbb{V}} \frac{G_0(\mathbf{r}_A,\mathbf{s})G_0^*(\mathbf{r}_B,\mathbf{s})}{|G_0(\mathbf{r}_B,\mathbf{s})|^2} d\mathbf{s}}_{D_{AB}^1}$$

$$+ \underbrace{\oint_{\partial\mathbb{V}} \frac{G_S(\mathbf{r}_A,\mathbf{s})G_0^*(\mathbf{r}_B,\mathbf{s})}{|G_0(\mathbf{r}_B,\mathbf{s})|^2} d\mathbf{s}}_{D_{AB}^2}$$

$$- \underbrace{\oint_{\partial\mathbb{V}} \frac{G_0(\mathbf{r}_A,\mathbf{s})G_0^*(\mathbf{r}_B,\mathbf{s})G_S(\mathbf{r}_B,\mathbf{s})}{|G_0(\mathbf{r}_B,\mathbf{s})|^2 G_0(\mathbf{r}_B,\mathbf{s})} d\mathbf{s}}_{D_{AB}^3}$$

(13)

Equation 13 shows that, to leading order in the scattered wavefield, the deconvolution integral in equation 10 can be represented by integrals D_{AB}^1 through D_{AB}^3. In fact, equation 13 is a Born-like approximation (e.g., Born and Wolf, 1959; Weglein et al., 2003) of equation 10. In contrast with $|G(\mathbf{r}_B,\mathbf{s})|^2$ in equation 10, $|G_0(\mathbf{r}_B,\mathbf{s})|^2$ in equation 13 does not contain cross terms between unperturbed and scattered wavefields. Therefore, $|G_0(\mathbf{r}_B,\mathbf{s})|^2$ is a slowly varying zero-phase function of $\mathbf{s}$; only the numerators determine the stationary-phase contributions to the integrals in the right-hand side of equation 13. This property allows direct comparison between the phase of integrands in equation 13 and terms in equation 5.

Physical insights into deconvolution interferometry come from observing that the integrands of D_{AB}^1 and D_{AB}^2 (equation 13) have the same phase as C_{AB}^1 and C_{AB}^2 in equations 4 and 5. Based on these observations and on equation 6 (Vasconcelos, 2007), we can conclude that D_{AB}^1 provides the causal and anticausal unperturbed wavefield that propagates from $\mathbf{r}_B$ to $\mathbf{r}_A$. More importantly, integrands of D_{AB}^2 and C_{AB}^2 have the same phase; it is controlled by $G_S(\mathbf{r}_A,\mathbf{s})G_0^*(\mathbf{r}_B,\mathbf{s})$. Thus, according to the representation theorem in Appendix A, D_{AB}^2 gives the causal scattered waves that are excited at $\mathbf{r}_B$ and recorded at $\mathbf{r}_A$.

We give a simple explanation of the causal nature of D_{AB}^2 for the special case of a classical scattering problem (e.g., Born and Wolf, 1959; Rodberg and Thaler, 1967), where G_0 is a transmitted wave and G_S contains the scattered waves. Scattered waves usually arrive at a later time than the direct wave. The phase of D_{AB}^2 is given by the traveltime difference $T_{S,A} - T_{0,B}$. (Here, $T_{S,A}$ is the arrival time of the scattered wave arriving at receiver A and $T_{0,B}$ is the arrival time of the direct wave at receiver B.) At the stationary point that yields a scattered wave propagating between $\mathbf{r}_B$ and $\mathbf{r}_A$, $T_{S,A} = T_{0,B} + T_{S,AB}$ (see Appendices A and C), where $T_{S,AB}$ is the traveltime of a scattered wave propagating from B to A. So the stationary phase of D_{AB}^2 is $\omega T_{S,AB}$.

In the process of deriving equation 13 (see equations 9–12), terms that carry the same phase as C_{AB}^3 and C_{AB}^4 do not appear in deconvolution interferometry. This implies that interferometry by deconvolu-

tion does not recover the anticausal scattering response between the two receivers, whereas correlation interferometry (equation 13) recovers both causal and anticausal scattered waves.

The term D_{AB}^3 has no counterpart in correlation interferometry. Because of their opposite sign, D_{AB}^3 and D_{AB}^2 in equation 13 cancel when $\mathbf{r}_A = \mathbf{r}_B$. As the offset between the two receivers increases, the sum $D_{AB}^2 + D_{AB}^3$ becomes nonzero. To address the physical significance of D_{AB}^3, it is useful to analyze the result of deconvolution interferometry when $\mathbf{r}_A = \mathbf{r}_B$. This consists of the zero-offset trace in the pseudoshot gather obtained by interferometry. From equation 9, it follows that in the frequency domain, $D_{BB} = 1$ (i.e., when $\mathbf{r}_A = \mathbf{r}_B$). Zero-offset deconvolution interferometry thus gives

$$D_{BB}(t) = \delta(t) \qquad (14)$$

in the time domain. Equation 14 states that, in deconvolution interferometry, scattered waves with nonzero traveltimes vanish at zero offset. This is an extra boundary condition imposed on the interferometric experiment in which waves are excited at $\mathbf{r}_B$ and recorded at $\mathbf{r}_A$. The consequence of this boundary condition is the creation of nonphysical events such as D_{AB}^3 that interfere destructively with scattered waves that arrive at zero offset with nonzero traveltimes.

We use Figure 1 to summarize the physics of the extra boundary condition imposed by deconvolution interferometry (equation 14). If G is the pressure response, we refer to this boundary condition in the interferometric experiment as the free-point boundary condition. We use this term because the physical meaning of this boundary condition is analogous to that of a free-surface boundary condition (where pressure is equal to zero), but instead it applies only to a point in space (in this case, $\mathbf{r}_B$). When G stands for particle-velocity response, the condition in equation 14 corresponds to clamping the point $\mathbf{r}_B$ so that it cannot move for $t \neq 0$. In that case, we refer to equation 14 as the clamped-point boundary condition. Throughout this paper, we use the term free-point when referring to the condition given by equation 14 because in previous equations G represents pressure waves (e.g., equations 3 and 6).

The effect of the free-point boundary condition is illustrated in Figure 1a for a 1D homogeneous medium. Starting at $x = x_0$ and $t = 0$, arrows in Figure 1a describe the path of a wave that propagates toward a scatterer at x_S and bounces off this scatterer to be scattered again at the free point at $x = x_0$. This wave continues to be scattered between x_S and x_0. As in the free-surface boundary condition, the free point at x_0 reflects, in one dimension, waves with reflection coefficient $r = -1$.

The extension of the free-point concept to 3D inhomogeneous media is shown in Figure 1b. In Figure 1b, a physical-scattered wave excited by the pseudosource $\mathbf{r}_B$ is recorded $\mathbf{r}_A$ with traveltime $t = t_1 + t_2$. The wave that is backscattered at $\mathbf{x}_S$ (Figure 1b) scatters once more at $\mathbf{r}_B$ because of the free-point boundary condition. The free-point scattered wave (dotted arrow) then travels directly to $\mathbf{r}_A$, where it is recorded with the traveltime $t = 2t_1 + t_3$. This arrival corresponds to term D_{AB}^3 in equation 13. When $\mathbf{r}_A = \mathbf{r}_B$, $t_2 = t_1$, and $t_3 = 0$, the singly and free-point scattered waves have the same traveltime. This agrees with our previous discussion on the phase of terms in equation 13. In this case, for a fixed $\mathbf{r}_B$ and variable $\mathbf{r}_A$, the traveltime of the free-point scattered wave is controlled only by t_3 because t_1 stays constant.

Note that t_3 is also the traveltime of the direct wave that travels from $\mathbf{r}_B$ to $\mathbf{r}_A$, which in turn is given by term D_{AB}^1 in equation 13. Because D_{AB}^3 is controlled by the direct-wave traveltime t_3 for a fixed $\mathbf{r}_B$, it has the same moveout as the direct wave in an interferometric shot

gather with a pseudosource at $\mathbf{r}_B$. This observation is valid for point scatterers but not for waves that scatter at an interface. For interface-scattered waves, all paths in Figure 1b would change with varying $\mathbf{r}_A$ (see the section on numerical examples). Figure 1b illustrates only one of the many free-point scattered waves produced by deconvolution interferometry (Appendix B). In contrast to physical waves, which are reflected specularly, waves scattered by the free-point boundary condition that constitute the spurious events are weaker in two or more dimensions than in one dimension because of geometric spreading.

Free-point scattered events such as D_{AB}^3 (equation 13) do not always result in artifacts in images produced from deconvolution interferometry. In Appendix B, we discuss the multiple scattering interactions that arise from the free-point boundary condition and their influence in imaging data reconstructed by deconvolution interferometry.

The role of wavefield separation

In previous sections, we learned that interferometry by direct deconvolution of measured data $u(\mathbf{r}_A, \mathbf{r})$ by $u(\mathbf{r}_B, \mathbf{r})$ (equation 9) imposes an extra boundary condition on waves excited by a pseudosource at $\mathbf{r}_B$ and recorded at $\mathbf{r}_A$. This free-point boundary condition generates additional undesired waves that can present a problem to imaging data reconstructed by deconvolution interferometry.

An alternative form of interferometry that does not generate the free-point scattered waves is given by the deconvolution of scattered waves with unperturbed waves:
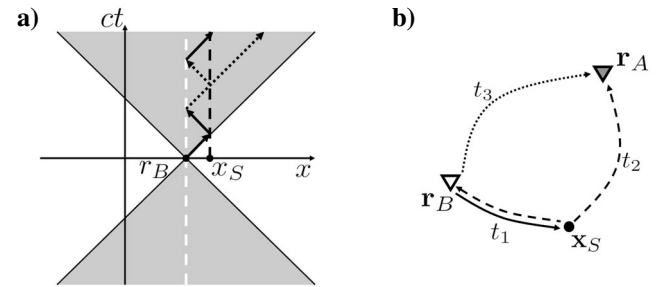

Figure 1. The free-point boundary condition in deconvolution interferometry. (a) Interpretation of the free-point boundary condition for 1D media with constant wave speed c. The gray area is where the wavefield is nonzero, r_B is the location of the receiver that acts as a pseudosource (and of the free-point), and x_S is the location of a point scatterer. Arrows represent waves, excited in r_B, propagating in the medium. Waves denoted with solid arrows propagate with opposite polarity with respect to waves represented by dotted arrows. The wavefield is equal to zero at the dashed white line, and the black vertical line indicates the region of influence of the scatterer at x_S. (b) The free-point boundary condition in a 3D inhomogeneous acoustic medium. The pseudosource, located at $\mathbf{r}_B$, is shown with the white triangle. The receiver is represented by the gray triangle at $\mathbf{r}_A$. The medium perturbation is a point scatterer at $\mathbf{x}_S$, denoted by the black circle. The solid arrow depicts a direct wave excited at $\mathbf{r}_B$. This wave is scattered at $\mathbf{x}_S$ and propagates toward $\mathbf{r}_A$ and $\mathbf{r}_B$, as shown by the dashed arrows. The dotted arrow denotes a free-point scattered wave recorded at $\mathbf{r}_A$. Waves represented by dashed and dotted arrows have opposite polarity. Labels t_1 through t_3 are the traveltimes of waves that propagate from $\mathbf{r}_B$ to $\mathbf{x}_S$, $\mathbf{x}_S$ to $\mathbf{r}_A$, and $\mathbf{r}_B$ to $\mathbf{r}_A$, respectively.

$$D'_{AB} = \frac{u_S(\mathbf{r}_A,\mathbf{s})}{u_0(\mathbf{r}_B,\mathbf{s})} = \frac{G_S(\mathbf{r}_A,\mathbf{s})}{G_0(\mathbf{r}_B,\mathbf{s})}. \qquad (15)$$

After summation over all sources $\mathbf{s}$ on $\partial\mathbb{V}$, this type of deconvolution interferometry yields only D_{AB}^2 in equation 13. Thus, it follows from our previous arguments regarding D_{AB}^2 (see Appendix A) that interferometry using equation 15 results only in the desired causal scattered waves $G_S(\mathbf{r}_A,\mathbf{r}_B)$. Although reconstructing causal and anticausal perturbed waves in $G(\mathbf{r}_A,\mathbf{r}_B)$ (e.g., using equation 3) can, in principle, correctly retrieve both the kinematic and dynamic wave behavior, reconstructing the causal $G_S(\mathbf{r}_A,\mathbf{r}_B)$ is likely to yield distorted amplitudes. This distortion arises from neglecting a volume integration (see Appendix A and Part 2).

To perform deconvolution interferometry according to equation 15, it is necessary to separate the wavefields $u_S(\mathbf{r}_A,\mathbf{r})$ and $u_0(\mathbf{r}_B,\mathbf{r})$ from recorded data $u(\mathbf{r}_A,\mathbf{r})$ and $u(\mathbf{r}_B,\mathbf{r})$, respectively. Different techniques are available in seismic interferometry to perform this separation. These techniques have different requirements and meet different objectives. Below we briefly discuss three such methods.

Direct-wave interferometry

One relatively simple way to perform wavefield separation required by equation 15 is to use recorded direct waves as u_0 and recorded data without the direct wave as u_S. This is the principle of the virtual source method presented by Bakulin and Calvert (2004, 2006) and Korneev and Bakulin (2006). The virtual source method of Bakulin and Calvert (2004, 2006) uses crosscorrelations along with a filter to account for the source spectrum, instead of the direct deconvolution in equation 15. Ramirez et al. (2007a) and Ramirez et al. (2007b) generalize the concept of direct-wave interferometry through a formalism based on Green's theorem, similar to ours in Appendix A and in Part 2.

In typical geophysical experiments, when the physical sources are above or at the same level as receivers and scattered waves come from below the sensors, direct-wave interferometry reconstructs only upgoing waves that scatter below receivers. When sensors are buried (e.g., a VSP or ocean-bottom survey) and the direct wave is not the only recorded downgoing wave, this type of interferometry can contain artifacts because of scattering above the receivers. Direct-wave interferometry requires a picking and subsequent windowing of direct waves, so it is only practical when the number of receivers is small (e.g., in a VSP survey), when direct-wave windowing is straightforward (e.g., in ocean-bottom surveys), and when the source-time function is sufficiently short that the direct wave does not interfere with reflected waves.

Dual-field separation

This type of wavefield separation relies on independent measurements of both the pressure wavefield u and particle velocity $(i\omega\rho)^{-1}\nabla u$ at the observation points. When such measurements are available, it is possible to separate upgoing from downgoing waves at any receiver point by summing and subtracting u and a suitable component of $(i\omega\rho)^{-1}\nabla u$ (e.g., Loewenthal and Robinson, 2000; Amundsen, 2001; Amundsen et al., 2001). Interferometry based on dual-sensor wavefield separation has a similar objective to that of direct-wave interferometry: It reconstructs upgoing waves propagating between $\mathbf{r}_B$ and $\mathbf{r}_A$ by the interference of upgoing waves recorded at $\mathbf{r}_A$ with downgoing waves recorded at $\mathbf{r}_B$.

Mehta et al. (2007a) extend the virtual source method of Bakulin and Calvert (2004, 2006) to include this type of wavefield separation, providing a field data example. Their approach uses crosscorrelations (e.g., as in equation 7) along with a source-shaping filter to extract waves propagating between receivers. Equation 15 can be used as an alternative to the method of Mehta et al. (2007a). In agreement with our analysis, Loewenthal and Robinson (2000) show that deconvolution of the upgoing with downgoing waves at a single receiver (i.e., set $\mathbf{r}_A = \mathbf{r}_B$ in equation 15) in a 1D medium results in the zero-offset reflectivity response $G_S(\mathbf{r}_B,\mathbf{r}_B)$.

The dual-field method of wavefield separation has the advantage that all downgoing waves can be used for interferometry, unlike direct-wave interferometry. However, it requires the simultaneous measurement of pressure and particle velocity, which is typically only available in four-component ocean-bottom cable seismic surveys.

Shot-domain wavefield separation

Up/down wavefield separation by either direct-wave windowing or dual-sensor summation generates interferometric sources that radiate energy toward one fixed direction (i.e., downward). Vasconcelos et al. (2007) devise a procedure to create pseudosources that radiate energy in a preferred direction. For example, for a subsalt walkaway VSP survey in a deviated well, recorded internal multiples can be used to image the salt structure from below with no knowledge of the salt velocity model (Vasconcelos et al., 2007).

This target-oriented interferometry approach selects arrivals in the shot domain based on their apparent shot-domain wavenumbers. The wavefield separation is given by

$$u_0(\mathbf{r}_B,\mathbf{r}) = \int \mathcal{H}_B(\mathbf{k}_{\mathbf{r}_B})u(\mathbf{k}_{\mathbf{r}_B},\mathbf{r})e^{i\mathbf{r}\mathbf{k}_{\mathbf{r}_B}}d\mathbf{k}_{\mathbf{r}_B} \qquad (16)$$

and

$$u_S(\mathbf{r}_A,\mathbf{r}) = \int \mathcal{H}_A(\mathbf{k}_{\mathbf{r}_A})u(\mathbf{k}_{\mathbf{r}_A},\mathbf{r})e^{i\mathbf{r}\mathbf{k}_{\mathbf{r}_A}}d\mathbf{k}_{\mathbf{r}_A}, \qquad (17)$$

where $\mathbf{k}_{\mathbf{r}_B}$ and $\mathbf{k}_{\mathbf{r}_A}$ are apparent shot-domain wave vectors (i.e., wave vectors measured directly from recorded shot gathers). Functions $\mathcal{H}_B$ and $\mathcal{H}_A$ are filters that select which portions of wave vectors $\mathbf{k}_{\mathbf{r}_B}$ and $\mathbf{k}_{\mathbf{r}_A}$ are kept. These filters carry out beam steering of the direct and scattered waves, respectively, used for interferometry. Integrals in equations 16 and 17 represent a multidimensional inverse Fourier transform that maps $\mathbf{k}_{\mathbf{r}_B} \mapsto \mathbf{r}_B$ and $\mathbf{k}_{\mathbf{r}_A} \mapsto \mathbf{r}_A$, respectively.

After the shot-domain directional filtering procedure described by equations 16 and 17, data are sorted into receiver gathers, which are then used for interferometry. In this approach, the choice of which sources $\mathbf{r}$ to use also influences wavefield separation. Our work shows that interferometry of wavefields using the wavefield separation according to equations 16 and 17 results in a pseudosource at $\mathbf{r}_B$ that radiates energy in the direction of the $\mathbf{k}_{\mathbf{r}_B}$ vectors preserved by the filter $\mathcal{H}_B$. In the interferometric experiment, waves recorded at $\mathbf{r}_A$ arrive in the $\mathbf{k}_{\mathbf{r}_A}$ directions determined by the choice of $\mathcal{H}_A$.

Apart from allowing for the design of pseudosources with a specific radiation property, this type of wavefield separation uses all arrivals with chosen directions for interferometry. We have shown that this method can be used in the interferometry of internal multiples to image salt structures from below. The main drawback of this method is that it cannot separate waves that propagate in the direction per-

pendicular to the receiver line/plane. So, for instance, it cannot do strictly up/down wavefield separation for data recorded in a horizontal line of receivers, although this is accomplished by the two prior wavefield separation methods. With four-component sensors, such a wavefield separation can be achieved even when waves propagate perpendicular to the array.

NUMERICAL EXAMPLE

The model we use is composed of a water layer with a wavespeed of 1500 m/s. A flat, horizontal interface is located at 2500-m depth. Contrast at the interface is produced by a velocity step from 1500 to 2200 m/s with a constant background density of 1000 kg/m^3. Receivers were positioned in a horizontal line at 750-m depth, starting at lateral position $x = 1500$ m and ending at 3000 m, with increments of 25 m. The source line also was horizontal at a depth of 400 m, ranging from $x = 500$ m to 4500 m, with increments of 50 m. Data were modeled by 2D acoustic finite differencing with absorbing boundary conditions. Figure 2 shows common-receiver gathers that consist of direct and single-reflected waves.

First, we use data in Figure 2 to analyze integrands in equations 3 and 10. Deconvolution of the wavefield in Figure 2a with the wavefield in Figure 2b yields Figure 3a; the crosscorrelation yields the field shown in Figure 3c. The deconvolution gather (Figure 3a) displays causal term D_{AB}^2, whereas both causal (C_{AB}^2) and anticausal (C_{AB}^3) contributions are present in the crosscorrelation gather (Figure 3c). This confirms our claim that deconvolution interferometry gives only causal scattering contributions. The term C_{AB}^4 also does not have a corresponding term in the deconvolution gather, as predicted by equation 13. Waveforms in Figure 3a are sharper than those in Figure 3c because deconvolution suppresses the source function. We use a water-level regularization method for deconvolutions (see Appendix A in Part 2).

Arrival times predicted with perturbation theory (bottom panels in Figure 3) provide an accurate representation of modeled results in the top panels of Figure 3. In particular, the deconvolution series (equation 12, Figure 3b) accurately describes deconvolution interferometry (equation 10, Figure 3a). As predicted, terms D_{AB}^2 and D_{AB}^3 have opposite polarity. The extrema of curves in Figure 3 are stationary source positions. Thus, the stationary traveltime of each term is the time associated to the extremum of its curve in Figure 3. The stationary traveltimes from D_{AB}^1 and C_{AB}^1 are at $t = \pm 1$ s, representing causal and anticausal direct waves. D_{AB}^2 and C_{AB}^2 result in a stationary time of approximately 2.5 s, which coincides with the traveltime of a causal single-scattered wave.
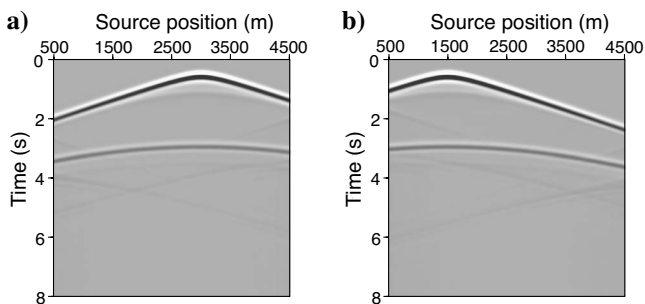
Other events present in the lower left-hand corner of Figure 3a are not present in Figure 3b. These events are described by higher-order terms of the deconvolution series (equation 12). Figure 4 shows how events are described by second- and third-order terms in the scattered wavefield. Events corresponding to third-order terms have considerably smaller amplitude than the ones related to second-order terms. Second-order terms are in turn weaker than the leading-order terms (Figure 3a). A decrease in the power of events with increasing order in the scattered wavefield is expected, given the expansion of equation 12. These examples confirm the accuracy of the deconvolution series in describing the results of using deconvolutions to perform interferometric reconstruction of acoustic wavefields (equation 10).

The integration over sources (e.g., equations 3 and 10) corresponds to the horizontal stack of plots in Figure 3a and c. For example, stacking Figure 3c results in a single trace that represents a wavefield excited at a lateral position of 1500 m and recorded at 3000 m. We create an interferometric shot gather with a pseudoshot placed at 1500 m by computing and stacking all deconvolution and crosscorrelation gathers (Figure 3a and c) for the receiver fixed at 1500 m but varying the lateral position of the other receiver from 1500 to 3000 m. Interferometric shot gathers are shown in Figure 5.

Both gathers in Figure 5 show both causal and anticausal direct waves. Only the gather produced from crosscorrelation (Figure 5b) shows causal and anticausal reflections, which agrees with equation 3. The interferometric gather produced from deconvolution interfer-
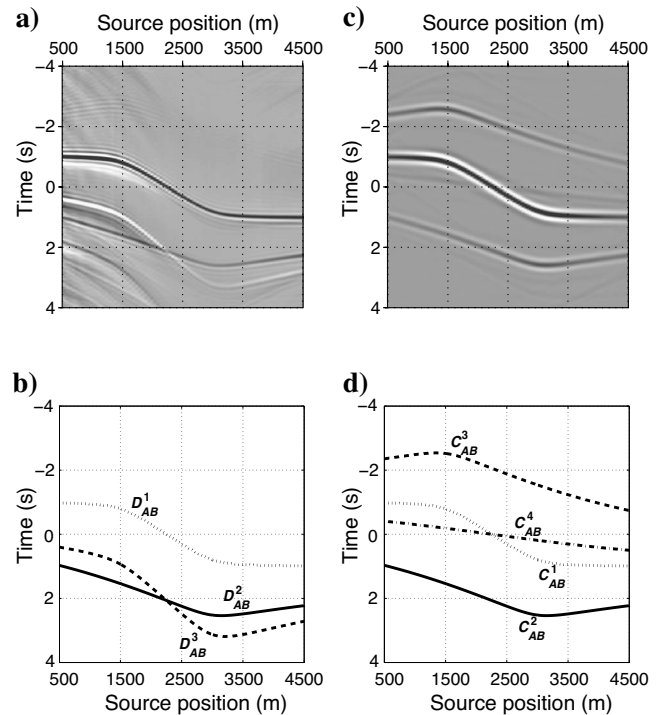
Figure 3. Deconvolution and crosscorrelation gathers for the first and last receivers, whose lateral positions are, respectively, 1500 and 3000 m. (a) The deconvolution gather obtained from deconvolving the common-receiver gather in Figure 2a with that in Figure 2b. (b) Ray-theoretical traveltimes for the terms in equation 13. (c) Analogous to (a), the crosscorrelations gather generated from source-by-source correlation of the two receiver gathers. (d) The asymptotic traveltimes corresponding to the phase of the integrands in equation 5.

Figure 2. Common-receiver gathers for receivers placed at (a) 3000 and (b) 1500 m.

ometry (Figure 5a) indeed shows only the causal scattered wave. The first-order term D_{AB}^3 (equation 13) can be seen in Figure 5a with opposite polarity and steeper-sloping character compared with the physical reflection. The reflection and the D_{AB}^3 spurious events converge at zero offset where they cancel. This is caused by the free-point boundary condition (equation 14) imposed by deconvolution interferometry. Other events are related to the truncated source integration (see the section titled Review of interferometry by crosscorrelations), such as the upward-sloping linear events appearing between the direct arrivals and reflections in all three gathers.

As discussed, the free-point spurious events can be avoided by different forms of wavefield separation. Although our objective is not to provide a detailed discussion of the effects of wavefield separation in interferometry, we briefly illustrate the effect of separating wavefields in this simple example in Figure 6. Results are an example of the direct-wave interferometry method.

By comparing deconvolution gathers in Figures 3a and 6c, we observe that only term D_{AB}^2 is recovered by interferometry after wave-
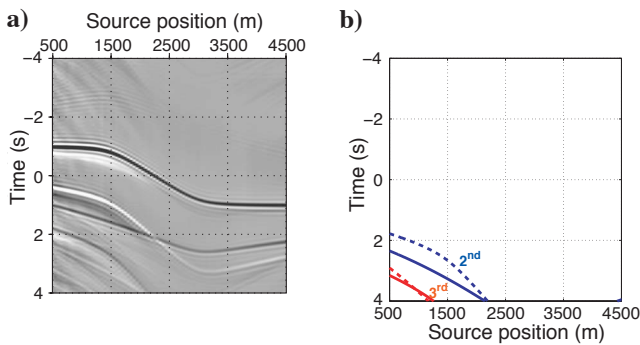
a) b)

Figure 4. Deconvolution interferometry terms that are nonlinear in the scattered wavefield. The left panel shows the integrand of the deconvolution interferometry integral (equation 10), computed from finite-difference modeling (same as in Figure 3a). In (b), solid- and dashed-blue curves represent the traveltimes corresponding to second-order terms that arise by setting $n = 1$ in equation B-5 and $n = 2$ in equation B-4, respectively. The solid and dashed red curves come from the phases of third-order terms that result from setting $n = 2$ in equation B-5 and $n = 3$ in equation B-4, respectively.
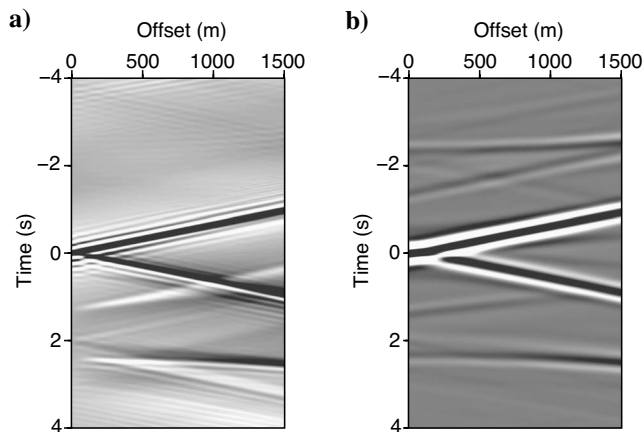
a) b)

Figure 5. Pseudoshot (interferometric) gathers with the shot positioned at the receiver at 1500 m. (a) Gather obtained by deconvolution interferometry (equation 10). (b) Gather generated by crosscorrelations (equation 3). Source integration of gathers in Figure 3a and c yields the last trace in (a) and (b), respectively.

field separation. Analogously, the correlation gather in Figure 6d recovers only term C_{AB}^2. Deconvolution and correlation gathers in Figure 6 demonstrate that direct-wave interferometry isolates the desired reflected wave in $G_S(\mathbf{r}_A, \mathbf{r}_B)$. The deconvolution gather in Figure 6c is wider band with respect to its correlation counterpart in Figure 6d because the source pulse is spiked naturally by deconvolution interferometry. The virtual source method of Bakulin and Calvert (2004, 2006) adds an additional source-shaping step to the calculation of correlation gathers in Figure 6d, which brings it closer to the response in Figure 6c.

Images obtained by shot-profile migration of gathers in Figure 5 are shown in Figure 7. The shot-profile migration was done by wavefield extrapolation with a split-step Fourier extrapolator (e.g., Stoffa et al., 1990). The reflector is placed at the correct depth of 2500 m in both images. The images are remarkably similar, despite differences between gathers in Figure 5. When compared with the image from correlation interferometry (Figure 7b), the deconvolution-based image (Figure 7a) does not show noticeable artifacts arising from spurious events produced by deconvolution interferometry. The only exception is a weak event with negative polarity at approximately 4-km depth in Figure 7a, which is not present in Figure 7b. This event is caused by a term that corresponds to setting $n = 1$ in equation B-5 (Appendix B). The effect of other free-point scattered waves cannot be seen in Figure 7a because they are weaker than the physically scattered primaries. For a more detailed discussion regarding multiple scattering caused by the free-point boundary condition, see Appendix B.

Ideally, the pseudoacquisition geometry (geometry of the receivers in the interferometry experiment) should be designed to reproduce offsets long enough to provide an image aperture comparable
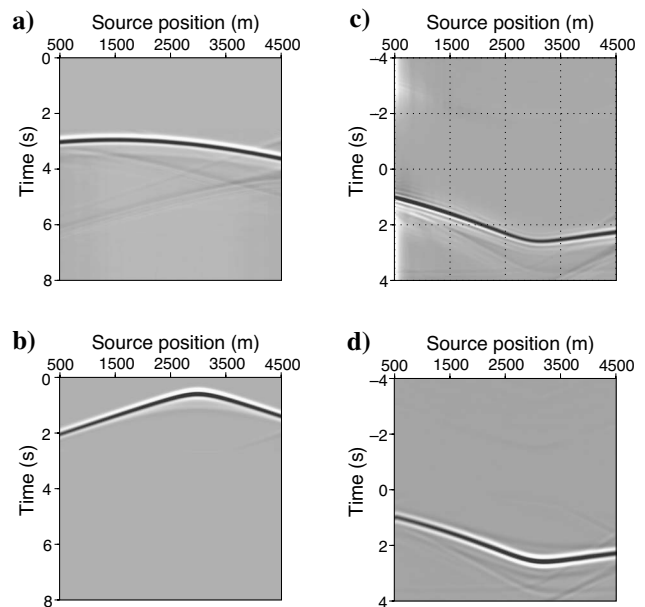
a) c)

b) d)

Figure 6. The role of wavefield separation on deconvolution and correlation interferometry. (a) The scattered wavefield $u_S(\mathbf{r}_A, \mathbf{s}, t)$ (i.e., wavefield perturbation) recorded at $\mathbf{r}_A$. Data in (b) consist of $u_0(\mathbf{r}_B, \mathbf{s}, t)$, the direct wave (i.e., the unperturbed wave) recorded at $\mathbf{r}_B$. The source-by-source deconvolution of data in (a) by that in (b) yields the deconvolution gather in (c), whereas (d) results from crosscorrelations.

to that of standard active-shot experiments. In that case, spurious arrivals produced by deconvolution interferometry can interfere destructively in the migration process (e.g., common shot or common offset) and not map coherently onto image artifacts (Appendix B). This is the case in the example in Figure 7.

DISCUSSION

Ideally, we want interferometry to give us the best possible representation of the impulse response between two given receivers. Crosscorrelation interferometry yields an accurate representation of waves propagating between receivers, but it requires additional processing to result in an impulsive response. Deconvolution interferometry yields an impulsive response, but it does so at the cost of generating artifacts. Another option is to design an inverse filter that generates a pseudosource with signature and radiation properties chosen by the user (J. Sheiman, personal communication, 2006). If there is some knowledge about the model, this tailor-made inverse filter can be designed to replicate an estimate of a desired wavefield (e.g., Amundsen, 2001). In this case, the output of the inverse filter approximates an impulsive version of crosscorrelation interferometry. The form of the deconvolution interferometry series is similar to that of scattering series such as the Lippmann-Schwinger (Rodberg and Thaler, 1967; Weglein et al., 2003). Forward- and inverse-scattering series serve, for instance, as the basis for methodologies in imaging and multiple suppression (e.g., Weglein et al., 2003; Malcolm et al., 2004). Hence, an inverse deconvolution interferometry series, in principle, could be devised for imaging pseudoshots generated by deconvolution interferometry.

There are other important potential applications for deconvolution interferometry. Deconvolution interferometry gives only causal wavefield perturbations, whereas unperturbed waves are present at both positive and negative times. For an ideal source coverage, subtracting the deconvolution-derived anticausal wavefield from the causal response results only in wavefield perturbations. This can be useful for processing data from time-lapse experiments as well as for preprocessing procedures such as direct- or surface-wave suppression. Apart from reconstructing pseudoshot experiments, interferometry can be applied to perform stable imaging in poorly known models (e.g., Borcea et al., 2005, 2006; Dussaud, 2005; Sava and Poliannikov, 2008). This type of interferometric imaging is done by crosscorrelations in the data domain (e.g., Borcea et al., 2005, 2006; Dussaud, 2005) or image domain (Sava and Poliannikov, 2008). The use of deconvolution in this type of interferometry application is likely to be worth pursuing as an alternative to the crosscorrelations used currently.

Numerical examples with impulsive source data show that deconvolution interferometry can successfully retrieve the causal response between two receivers. This response can be used to build interferometric shot gathers that, in turn, can be imaged. Imaging of deconvolution interferometric shot gathers shows that most of the free-point scattered waves do not map onto images. The free-point boundary condition in deconvolution interferometry makes the dynamics of the interferometric experiment different from a real experiment in which a source is placed at the receiver point. This means that data reconstructed by deconvolution interferometry are suitable for structural imaging but not for conventional amplitude analyses (e.g., amplitude-variation-with-offset analysis). However, in principle, it is possible to design an inverse-scattering procedure using the deconvolution series presented here to extract meaningful amplitudes from data reconstructed by deconvolution interferometry.
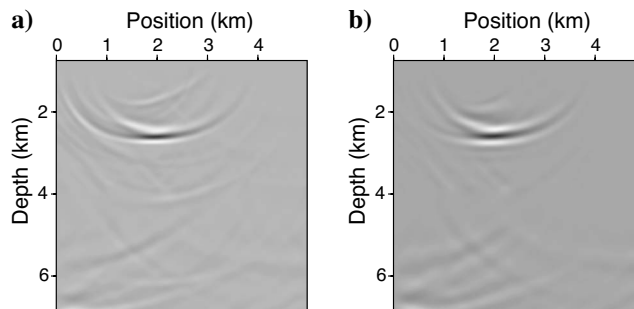

Figure 7. Shot-profile wave-equation migrated images of the pseudoshot gathers in Figure 5. (a, b) Images obtained from migrating the gathers in Figure 5a and b, respectively. The true depth of the target interface is 2500 m. The shot is placed at 1.5 km, and receivers cover a horizontal line from 1.5 to 3.0 km. Because the image is from a single shot placed at $x = 1500$ m and receivers placed at $1500 < x < 3000$ m, only a small portion of the reflector is seen at $z = 2500$ m and $1500 < x < 2500$ m.

CONCLUSION

By representing recorded wavefields as a superposition of transmitted and scattered wavefields, we derive a series expansion that describes deconvolution interferometry of receiver gathers before summing over sources. This derivation shows that interferometry by deconvolution, before stacking over sources, gives only the causal scattered wavefield, as if one receiver acted as a source. Because deconvolution interferometry requires the zero-offset wavefield to vanish at nonzero times, it generates spurious events to cancel scattered arrivals at zero offset. We refer to this condition as the free-point boundary condition at the pseudosource location. The deconvolution interferometry series we derive here provides a detailed physical description of what we refer to as free-point scattering. Unlike previously described spurious arrivals in interferometry, free-point scattered waves do not arise from the truncation of the surface integral or from the far-field approximation invoked commonly in interferometry. They are a consequence of using the deconvolution operator in interferometry.

Our goal is to demonstrate the feasibility of using deconvolutions to recover the impulse response between receivers. Deconvolution interferometry has proven to be an important tool for interferometric imaging from complicated excitation such as coda waves from earthquakes. In other applications, the complicated character of the excitation can be related to the source itself. One such example is drill-bit seismology. When independent measures of the drill-bit stem noise are not available, deconvolution interferometry is necessary. This is the focus of Part 2.

Other important applications for deconvolution interferometry can arise when wavefield separation methods are used along with interferometry. In this context, we found deconvolution interferometry to be a useful tool for imaging internal multiples in VSP experiments. We also believe that deconvolution interferometry can play an important role in interferometric imaging of OBC data, but this topic is the subject of ongoing research.

ACKNOWLEDGMENTS

APPENDIX A

A REPRESENTATION THEOREM IN PERTURBED ACOUSTIC MEDIA

The claim that terms such as C_{AB}^2 (equation 5) and D_{AB}^2 (equation 13) yield causal scattered waves in arbitrarily heterogeneous acoustic media comes from a representation theorem in perturbed media (Vasconcelos, 2007). From the derivation in Vasconcelos (2007), we reproduce here only those aspects of immediate relevance to interferometry.

Let p and $\mathbf{v}$ be pressure and particle velocity, which obey the wave-equation systems for unperturbed and perturbed media, respectively, given by

$$\nabla p_0^A(\mathbf{r},\omega) - i\omega\rho_0(\mathbf{r})\mathbf{v}_0^A(\mathbf{r},\omega) = 0$$
$$\nabla \cdot \mathbf{v}_0^A(\mathbf{r},\omega) - i\omega\kappa_0(\mathbf{r})p_0^A(\mathbf{r},\omega) = q^A(\mathbf{r},\omega)$$
$$(A\text{-}1)$$

and

$$\nabla p^A(\mathbf{r},\omega) - i\omega\rho(\mathbf{r})\mathbf{v}^A(\mathbf{r},\omega) = 0$$
$$\nabla \cdot \mathbf{v}^A(\mathbf{r},\omega) - i\omega\kappa(\mathbf{r})p^A(\mathbf{r},\omega) = q^A(\mathbf{r},\omega),$$
$$(A\text{-}2)$$

where κ and ρ are the compressibility and density, respectively. As in the main text, subscript zero denotes unperturbed quantities whereas its absence indicates perturbed quantities. Thus, $p = p_0 + p_S$ and $\mathbf{v} = \mathbf{v}_0 + \mathbf{v}_S$, where the fields with subscript S are perturbations (e.g., scattered waves). The source term q is of the volume injection-rate density type. Superscript A indicates a particular wave state (Vasconcelos, 2007).

By isolating the interaction quantity $\nabla \cdot (p^A\mathbf{v}_0^{B*} + p_0^{B*}\mathbf{v}^A)$, we derive the following correlation reciprocity theorem in perturbed media (Vasconcelos, 2007):

$$\oint_{\partial\mathbb{V}} \left[p_S^A\mathbf{v}_0^{B*} + p_0^{B*}\mathbf{v}_S^A \right] \cdot d\mathbf{S}$$
$$= \int_{\mathbb{V}} p_S^A q_0^{B*}dV - \int_{\mathbb{V}} i\omega(\kappa_0 - \kappa)p^A p_0^{B*}dV, \qquad (A\text{-}3)$$

which relates perturbed waves in state A with unperturbed ones in state B. To obtain a representation theorem from equation A-2, we define states A and B by setting

$$q^{A,B} = \delta(\mathbf{r} - \mathbf{r}_{A,B}) \qquad (A\text{-}4)$$

and

$$p^{A,B}(\mathbf{r},\omega) = G(\mathbf{r},\mathbf{r}_{A,B},\omega)$$
$$= G_0(\mathbf{r},\mathbf{r}_{A,B},\omega) + G_S(\mathbf{r},\mathbf{r}_{A,B},\omega). \quad (A\text{-}5)$$

Using definitions in equations A-4 and A-5 in equation A-3 yields the representation theorem,

$$G_S(\mathbf{r}_B,\mathbf{r}_A) = \oint_{\partial\mathbb{V}} \frac{1}{i\omega\rho}\Big[G_S(\mathbf{r},\mathbf{r}_A) \nabla G_0^*(\mathbf{r},\mathbf{r}_B)$$
$$+ G_0^*(\mathbf{r},\mathbf{r}_B) \nabla G_S(\mathbf{r},\mathbf{r}_A) \Big] \cdot d\mathbf{S}$$
$$+ \int_{\mathbb{V}} i\omega(\kappa_0 - \kappa)G(\mathbf{r},\mathbf{r}_A)G_0^*(\mathbf{r},\mathbf{r}_B)dV.$$
$$(A\text{-}6)$$

Equation A-6 is exact and holds for arbitrary medium properties and experiment geometries. For simplicity, we use equation A-6 in our discussion. This equation is strictly valid when perturbations occur only in compressibility, but it can be extended to account for density perturbations as well (Vasconcelos, 2007, Vasconcelos and Snieder, 2008).

Equation A-6 describes how to reconstruct causal scattered waves propagating from $\mathbf{r}_B$ to $\mathbf{r}_A$. In its exact form, equation A-6 is impractical for seismic interferometry because it requires (1) dipole sources along $\partial\mathbb{V}$ or dual-field measurements at $\mathbf{r}_B$ and $\mathbf{r}_A$ and (available in some cases) (2) sources and knowledge of the medium perturbations inside the volume $\mathbb{V}$. When the requirement cannot be met, equation A-6 can be adapted for interferometry with pressure measurements alone. This is done typically with a far-field radiation boundary condition, by making approximation $(\nabla G)\cdot\mathbf{n} = i\omega c^{-1}G$ (Wapenaar and Fokkema, 2006; Vasconcelos, 2007). This results in

$$G_S(\mathbf{r}_B,\mathbf{r}_A) = \oint_{\partial\mathbb{V}} \frac{2}{\rho c}G_S(\mathbf{r},\mathbf{r}_A)G_0^*(\mathbf{r},\mathbf{r}_B)d\mathbf{S}$$
$$+ \int_{\mathbb{V}} i\omega(\kappa_0 - \kappa)G_0(\mathbf{r},\mathbf{r}_A)G_0^*(\mathbf{r},\mathbf{r}_B)dV$$
$$+ \int_{\mathbb{V}} i\omega(\kappa_0 - \kappa)G_S(\mathbf{r},\mathbf{r}_A)G_0^*(\mathbf{r},\mathbf{r}_B)dV.$$
$$(A\text{-}7)$$

We separate the volume integral in equation A-6 into two volume integrals in equation A-7 using identity $G^A = G_0^A + G_S^A$. In equation A-7, the surface integral plays the role of terms C_{AB}^2 (equation 5) and D_{AB}^2 (equation 13). For a given stationary point, say, $\mathbf{r}_1$, that reconstructs scattered waves in $G_S(\mathbf{r}_B,\mathbf{r}_A)$ (Figure A-1), the first volume integral accounts for perturbations in the paths of $G_0(\mathbf{r},\mathbf{r}_A)$ and $G_0(\mathbf{r},\mathbf{r}_B)$ (i.e., along the solid arrows in Figure A-1). When receivers are located between the sources and scatterers as illustrated by Figure A-1, the first volume integral in equation A-7 is equal to zero because $\kappa_0 - \kappa = 0$ along the paths of $G_0(\mathbf{r},\mathbf{r}_A)$ and $G_0(\mathbf{r},\mathbf{r}_B)$ (i.e., the solid arrows are not affected by perturbations in $\mathbb{P}$).

The second volume integral in equation A-7 results in a term with the same phase as that resulting from the surface integral but with different amplitude. Vasconcelos (2007) shows that the term resulting from the second volume integral is weaker than that resulting from the surface integral; generally, the second volume integral can

be ignored for perturbation and receiver configurations as in Figure A-1. Thus, for experiments such as the one shown in Figure A-1, equation A-7 can be reduced to

$$G_S(\mathbf{r}_B, \mathbf{r}_A) \approx \int_{\partial \mathbb{V}_1} \frac{2}{\rho c} G_S(\mathbf{r}, \mathbf{r}_A) G_0^*(\mathbf{r}, \mathbf{r}_B) d\mathbf{S}, \quad \text{(A-8)}$$

which shows why term D_{AB}^2 (equation A-7), and thus deconvolution interferometry, yields only causal scattered waves.

Equation A-8 is analogous to those in the main text by setting $\mathbf{r} = \mathbf{s}$ and using source-receiver reciprocity. The term $\partial \mathbb{V}_1$ is a segment of the $\partial \mathbb{V}$ surface, chosen such that the first volume integral in equation A-7 goes to zero. The experiment configuration in Figure A-1 is adequate to describe interferometry from seismic surveys because, in typical seismic acquisition designs, receivers lie between the sources and the subsurface target. Equation A-8 is only valid in the context of Figure A-1; otherwise, the volume integrals in equation A-7 cannot be neglected. Vasconcelos (2007) discusses the effects of these volume integrals for situations other than for that in Figure A-1 as well as their role in attenuative media.

Equation A-8 provides the physical basis for use of two-way wavefield separation in interferometry. When u_0 and u_S can be separated from the recorded u, the direct evaluation of an integral, such as that in equation A-8, becomes practical. Refer to the main text in which we offer a more detailed account on the role of wavefield separation in seismic interferometry.

APPENDIX B

MULTIPLE FREE-POINT SCATTERING

In Appendix A, we limited our analysis of the deconvolution interferometry series to first-order terms in G_S. Here, we analyze the higher-order terms, which describe multiple free-point scattering interactions. We first show the connection between the deconvolution interferometry series in equation 12 and the Lippmann-Schwinger scattering series (Lippmann, 1956; Rodberg and Thaler, 1967), given by

$$G_S(\mathbf{r}_A, \mathbf{s}) = \sum_{n=1}^{\infty} \int_{\mathbb{V}} G_0(\mathbf{r}_A, \mathbf{r}_n) V(\mathbf{r}_n)$$
$$\times G_0(\mathbf{r}_n, \mathbf{r}_{n-1}) \ldots V(\mathbf{r}_1) G_0(\mathbf{r}_1, \mathbf{s}) d\mathbf{r}_n \ldots d\mathbf{r}_1,$$
$$\text{(B-1)}$$

where $V(\mathbf{r})$ is the perturbation operator or scattering potential (Rodberg and Thaler, 1967; Weglein et al., 2003). For acoustic waves with unperturbed density, $V(\mathbf{r}) = \omega^2[c^{-2}(\mathbf{r}) - c_0^{-2}(\mathbf{r})]$, with c and c_0 being the perturbed and unperturbed wave speeds, respectively. Equation B-1 can be written in operator form as

$$G_S(\mathbf{r}, \mathbf{s}) = \mathcal{G}_0(\mathbf{r}, \mathbf{s}) \sum_{n=1}^{\infty} (\mathcal{V}(\mathbf{r}) \mathcal{G}_0(\mathbf{r}, \mathbf{s}))^n. \quad \text{(B-2)}$$

Equation 12 can be written in a form similar to that of equation B-2, i.e.,

$$D_{AB} = \frac{G(\mathbf{r}_A, \mathbf{s})}{G_0(\mathbf{r}_B, \mathbf{s})} \sum_{n=0}^{\infty} (-1)^n \left(\frac{G_S(\mathbf{r}_B, \mathbf{s})}{G_0(\mathbf{r}_B, \mathbf{s})}\right)^n. \quad \text{(B-3)}$$

For $n = 1$, the Lippmann-Schwinger (equation B-2) series yields the Born approximation; whereas the Born-like approximation in deconvolution interferometry series gives equation 13. Any term in equation B-2 describes n interactions (i.e., nth-order scattering) between G_0 and the medium perturbation (i.e., the scatterers) represented by $V(\mathbf{r})$. Likewise, terms with $n \neq 0$ in equation B-3 describe n interactions between the waves in $G(\mathbf{r}_A, \mathbf{s}) G_0^{-1}(\mathbf{r}_B, \mathbf{s})$ and those in $G_S(\mathbf{r}_B, \mathbf{s}) G_0^{-1}(\mathbf{r}_B, \mathbf{s})$. Note that the interactions described by equation B-2 are actual physical interactions, whereas the free-point interactions described by equation B-3 are artificial interactions imposed by the free-point boundary condition in deconvolution interferometry.

It follows from equation B-3 that for the classical scattering case where G_S denoted scattered or reflected waves that arrive after the direct wave, all free-point scattered waves are causal. In the main text (along with Appendices A and C), we show that all of the physical scattered waves reconstructed by deconvolution interferometry are causal (i.e., they are recorded at positive times). Because the free-point scattered waves must cancel physical scattered waves arriving at zero offset, the zero-offset traveltime of the free-point scattered waves is always positive.

Furthermore, in the classical scattering problem (see Appendix A), the traveltime of any scattered wave is larger than the traveltime of the corresponding unperturbed wave, thus $T_{S,B} - T_{0,B} > 0$. Therefore, according to equation 12, if traveltimes in the first term are given by $T_{A,B} - T_{0,B}$, then it follows from the second term that $T_A - T_{0B} + n(T_{SB} - T_{0B}) > T_A - T_{0B}$. Thus, the finite-offset traveltime of the free-point scattered waves is always larger than that of the physical scattered waves. With causal zero-offset traveltimes and finite-offset arrival times larger than those of physical scattered waves, free-point scattered are always causal.

Let us consider the second term on the right-hand side of equation 12 and perform the integration over sources according to equation 10. Next, using the Lippmann-Schwinger series (equation B-2) and identity $G(\mathbf{r}_A, \mathbf{s}) = G_0(\mathbf{r}_A, \mathbf{s}) + G_S(\mathbf{r}_A, \mathbf{s})$, we can distinguish two types of free-point scattering interactions. One is described by
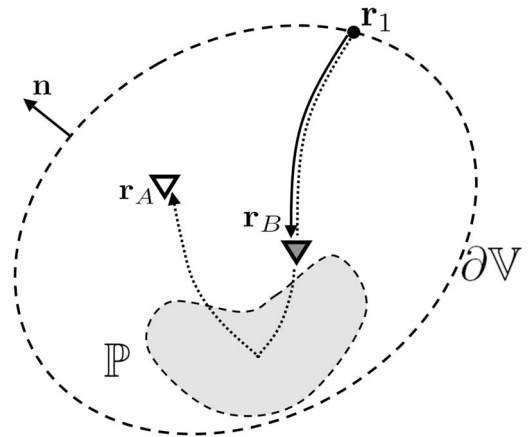

Figure A-1. Special case in perturbation-based interferometry. The wavefield perturbation $G_S(\mathbf{r}_A, \mathbf{r}_B)$ can be reconstructed by crosscorrelating $G(\mathbf{r}_A, \mathbf{s})$, wavefield perturbations recorded at $\mathbf{r}_A$ (represented by the dotted arrow), with $G_0(\mathbf{r}_B, \mathbf{s})$, the unperturbed waves recorded at $\mathbf{r}_B$ (denoted by the solid arrow). The point $\mathbf{r}_1$ is a stationary source point that gives rise to the primary scattered wave propagating from $\mathbf{r}_B$ to $\mathbf{r}_A$.

$$\mathcal{I}_{\text{fp,I}} = \oint_{\partial V} \frac{G_0(\mathbf{r}_A,\mathbf{s})}{G_0(\mathbf{r}_B,\mathbf{s})} \sum_{n=1}^{\infty} (-1)^n \left(\frac{G_S(\mathbf{r}_B,\mathbf{s})}{G_0(\mathbf{r}_B,\mathbf{s})} \right)^n d\mathbf{s}$$

$$= \oint_{\partial V} \frac{G_0(\mathbf{r}_A,\mathbf{s})}{G_0(\mathbf{r}_B,\mathbf{s})} \sum_{n=1}^{\infty} (-1)^n$$

$$\times \left(\frac{\sum_{m=1}^{\infty} \mathcal{G}_0(\mathbf{r}_B,\mathbf{s})(\mathcal{V}(\mathbf{r}_B)\mathcal{G}_0(\mathbf{r}_B,\mathbf{s}))^m}{G_0(\mathbf{r}_B,\mathbf{s})} \right)^n d\mathbf{s}$$

$$(B\text{-}4)$$

and the other by

$$\mathcal{I}_{\text{fp,II}} = \oint_{\partial V} \frac{G_S(\mathbf{r}_A,\mathbf{s})}{G_0(\mathbf{r}_B,\mathbf{s})} \sum_{n=1}^{\infty} (-1)^n \left(\frac{G_S(\mathbf{r}_B,\mathbf{s})}{G_0(\mathbf{r}_B,\mathbf{s})} \right)^n d\mathbf{s}$$

$$= \oint_{\partial V} \frac{\mathcal{G}_0(\mathbf{r}_A,\mathbf{s}) \sum_{p=1}^{\infty} (\mathcal{V}(\mathbf{r}_A)\mathcal{G}_0(\mathbf{r}_A,\mathbf{s}))^p}{G_0(\mathbf{r}_B,\mathbf{s})}$$

$$\times \sum_{n=1}^{\infty} (-1)^n$$

$$\times \left(\frac{\sum_{m=1}^{\infty} \mathcal{G}_0(\mathbf{r}_B,\mathbf{s})(\mathcal{V}(\mathbf{r}_B)\mathcal{G}_0(\mathbf{r}_B,\mathbf{s}))^m}{G_0(\mathbf{r}_B,\mathbf{s})} \right)^n d\mathbf{s}.$$

$$(B\text{-}5)$$

The sum of these two integrals, $\mathcal{I}_{\text{fp,I}} + \mathcal{I}_{\text{fp,II}}$, gives the surface integral of the second term in equation 12. Integrals $\mathcal{I}_{\text{fp,I}}$ (equation B-4) and $\mathcal{I}_{\text{fp,II}}$ describe two distinct types of free-point scattering interactions, which we refer to as type 1 and type 2.

The physics of these two types of free-point scattering interactions are illustrated in Figure B-1. Type 1 interactions are shown in Figure B-1a, and type 2 interactions are represented in Figure B-1b. The type 1 interaction is the same as in the example we used to describe the free-point scattering effect in Figure 1b. In both types of interaction (Figure B-1), physical waves excited by the pseudosource at $\mathbf{r}_B$ (solid arrow) bounce at the scatterer at $\mathbf{x}_S$ (dashed arrow) and then scatter off the free point at $\mathbf{r}_B$. The difference between type 1 and type 2 interactions lies in what happens to the waves after scattering at the free point. In the type 1 interaction (Figure B-1a), the free-point scattered wave (dotted black arrow) travels to the receiver
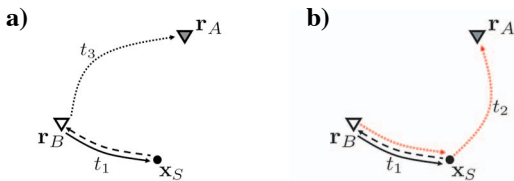

Figure B-1. The two types of free-point scattering interactions in deconvolution interferometry. Here, as in Figure 1b, solid arrows indicate the outgoing waves excited by the pseudosource at $\mathbf{r}_B$, dashed arrows represent physically scattered waves, and dotted arrows denote the free-point scattered waves. In (a), the free-point scattered wave (dotted black arrow) travels from $\mathbf{r}_B$ to $\mathbf{r}_A$ without interacting with any scatterers. The other type of interaction is shown in (b), in which the free-point scattered wave (dotted red arrow) interacts with the scatterer at $\mathbf{x}_S$ before being recorded at $\mathbf{r}_A$.

at $\mathbf{r}_A$ without interacting with the scatterer at $\mathbf{x}_S$. After the free-point scattering at $\mathbf{r}_B$, type 2 waves (Figure B-1b, dotted red arrow) first interact with the scatterer at $\mathbf{x}_S$ and then are recorded at $\mathbf{r}_A$.

When the scattering properties are arbitrary (i.e., many scatterers of arbitrary size, shape, and scattering strength), the second line in equation B-4 says that type 1 waves are described by m interactions of waves excited at $\mathbf{r}_B$ with the scatterers, interacting n times with the free-point scatterer. Under the same conditions, type 2 waves (equation B-5) are described by waves departing from the pseudosource at $\mathbf{r}_B$ that interact m times with the scatterers, interact n times with the free-point, and again interact with the medium p times before being recorded at $\mathbf{r}_A$.

Two important physical observations must be made regarding the free-point scattering interactions. First, when the objective is ultimately to image primary reflections from deconvolution interferometry (see Appendix A), the type 2 free-point scattered waves (e.g., Figure B-1b) can result in image artifacts because their moveout can be close to that of physical primaries. For examples in Figures 1b and B-1b, the primary and free-point scattered moveout are the same for constant $(\mathbf{r}_B,\mathbf{x}_S)$ and varying $\mathbf{r}_A$. When the scattering occurs at interfaces (i.e., reflectors), the difference between the moveout of primaries and free-point scattered waves increases as $\mathbf{r}_A$ is placed farther from $\mathbf{r}_B$. This occurs because, for interface-scattered waves, all paths in Figure B-1 change with fixed $\mathbf{r}_B$ and varying $\mathbf{r}_A$.

The second important remark concerning the free-point scattered waves is that for any given value of n, the type 2 waves (equation B-5) are one order higher in the scattered wavefields G_S with respect to the type 1 waves (equation B-4). Therefore, at a given n interaction with the free-point (see equations B-4 and B-5), type 1 waves are always stronger than their type 2 counterpart.

APPENDIX C

NUMERICAL ANALYSIS OF THE FREE-POINT SCATTERED WAVES

The main objective in studying spurious terms such as D_{AB}^3 is to determine their influence in imaging data from deconvolution interferometry. Once a model is specified, we compute the ray-based traveltimes of each spurious arrival for all source positions according to equations B-4 and B-5. From the maxima of the phases of each spurious event, we determine their corresponding stationary traveltime and source position. We do this for a fixed position $\mathbf{r}_B$ as a function of a laterally varying $\mathbf{r}_A$. Given the receiver positions, stationary traveltimes, and model parameters, we predict the imaged depth of any given term (e.g., D_{AB}^2) through common-shot migration (Bleistein et al., 2001). The result of this analysis is shown in Figure C-1. Geometry and model parameters used in computations in Figure C-1 are the same as in the numerical model we discuss in the main text. For these computations, $\mathbf{r}_A$ and $\mathbf{r}_B$ are kept at the same constant depth level.

Only term D_{AB}^2 represents physical scattered waves in Figure C-1. As expected, D_{AB}^2 is mapped at the same depth for all offsets, as shown by the solid black line in the figure. On the other hand, the spurious terms in Figure C-1 map to depths that increase with increasing offset. This suggests that when a sufficiently large range of offsets is used, most spurious events interfere destructively when imaged. The only exception is the type 2 free-point term that corresponds to $n = 1$ in equation B-5 whose mapped depth varies slowly with offset. This happens because type 2 free-point scattered waves
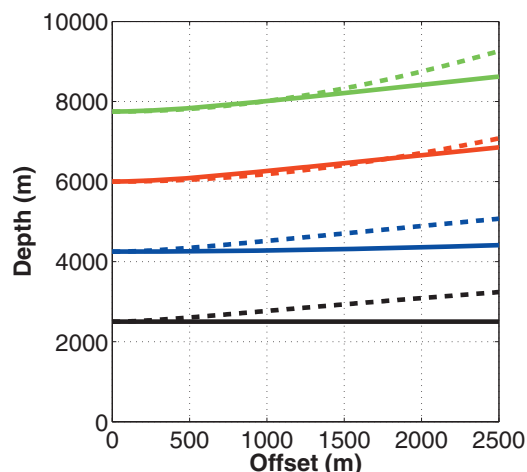
Figure C-1. Depths obtained by shot-profile migration of stationary traveltimes of deconvolution interferometry terms with varying receiver-to-receiver offset. Black lines correspond to the terms that are of leading order in the scattered wavefield. The solid black line represents migrated depths from traveltimes associated with term D_{AB}^2 (equation 13); the dashed black line pertains to term D_{AB}^3 (also equation 13). The blue, red, and green curves are associated, respectively, with quadratic, cubic, and quartic terms with respect to scattered waves. For a given order in the scattered waves, we show only the two terms that have strongest amplitude. Of the blue curves, the solid curve relates to the $n = 1$ in equation B-5 and the dashed one pertains to $n = 2$ in equation B-4. The imaged depths in red (i.e., the terms cubic on the scattered fields) are computed from setting $n = 2$ in equation B-5 and $n = 3$ in equation B-4. The quartic terms come from equation B-5 for $n = 3$ and equation B-4 for $n = 4$.

can behave as physical multiples; thus, their moveout can be close to that of primary reflections (see main text and Figure B-1).

Events corresponding to solid and dashed lines of a common color in Figure C-1 have opposite polarity (see equations B-4 and B-5). Hence, these events cancel as they approach zero offset. At zero offset (Figure C-1), second-order spurious events map at twice the depth of the physical reflector relative to the receivers (receiver depth is 750 m), third-order events map at three times that depth, and so on. This observation can be verified by setting $\mathbf{r}_A = \mathbf{r}_B$ in the terms from equations B-4 and B-5 that correspond to solid and dashed curves of a given color in Figure C-1.

REFERENCES

Amundsen, L., 2001, Elimination of free-surface related multiples without need of the source wavelet: Geophysics, **66**, 327–341.
Amundsen, L., L. T. Ikelle, and L. E. Berg, 2001, Multidimensional signature deconvolution and free-surface multiple elimination of marine multicomponent ocean-bottom seismic data: Geophysics, **66**, 1594–1604.
Bakulin, A., and R. Calvert, 2004, Virtual source: New method for imaging and 4D below complex overburden: 74th Annual International Meeting, SEG, Expanded Abstracts, 2477–2480.
——, 2006, The virtual source method: Theory and case study: Geophysics, **71**, no. 4, SI139–SI150.
Berkhout, A. J., and D. J. Verschuur, 2006, Imaging of multiple reflections: Geophysics, **71**, no. 4, SI209–SI220.
Bleistein, N., J. K. Cohen, and J. W. Stockwell, Jr., 2001, Mathematics of multidimensional seismic imaging, migration, and inversion: Springer Publishing Company, Inc.
Bleistein, N., and R. A. Handelsman, 1975, Asymptotic expansions of integrals: Dover Publishing, Inc.
Borcea, L., G. Papanicolau, and C. Tsogka, 2005, Interferometric array imaging in clutter: Inverse Problems, **21**, 1419–1460.
——, 2006, Coherent interferometric imaging in clutter: Geophysics, **71**,

no. 4, SI165–SI175.
Born, M., and E. Wolf, 1959, Principles of optics: Cambridge University Press.
Curtis, A., P. Gerstoft, H. Sato, R. Snieder, and K. Wapenaar, 2006, Seismic interferometry — Turning noise into signal: The Leading Edge, **25**, 1082–1092.
Draganov, D., K. Wapenaar, and J. Thorbecke, 2006, Seismic interferometry: Reconstructing the earth's reflection response: Geophysics, **71**, no. 4, SI61–SI70.
Dussaud, E., 2005, Velocity analysis in the presence of uncertainty: Ph.D. dissertation, Rice University.
Fink, M., 2006, Time-reversal acoustics in complex environments: Geophysics, **71**, no. 4, SI151–SI164.
Halliday, D., A. Curtis, D. van Mannen, and J. Robertsson, 2007, Interferometric surface wave (ground roll) isolation and removal: Geophysics, **72**, no. 5, A69–A73.
Holvik, E., and L. Amundsen, 2005, Elimination of the overburden response from multicomponent source and receiver seismic data, with source designature and decomposition into PP-, PS-, SP-, and SS-wave responses: Geophysics, **70**, no. 2, S43–S59.
Korneev, V., and A. Bakulin, 2006, On the fundamentals of the virtual source method: Geophysics, **71**, no. 3, A13–A17.
Larose, E., L. Margerin, A. Derode, B. van Tiggelen, M. Campillo, N. Shapiro, A. Paul, L. Stehly, and M. Tanter, 2006, Correlation of random wavefields: An interdisciplinary review: Geophysics, **71**, no. 4, SI11–SI21.
Lippmann, B. A., 1956, Rearrangement collisions: Physics Review, v. **102**, 264–268.
Lobkis, O. I., and R. L. Weaver, 2001, On the emergence of the Green's function in the correlations of a diffuse field: Journal of the Acoustical Society of America, **110**, 3011–3017.
Loewenthal, D., and E. A. Robinson, 2000, On unified dual wavefields and Einstein deconvolution: Geophysics, **65**, 293–303.
Malcolm, A., J. Scales, and B. A. van Tiggelen, 2004, Extracting the Green's function from diffuse, equipartitioned waves: Physical Review E, **70**, 015601.
Mehta, K., A. Bakulin, J. Sheiman, R. Calvert, and R. Snieder, 2007a, Improving the virtual source method by wavefield separation: Geophysics, **72**, no. 4, V79–V86.
Mehta, K., R. Snieder, and V. Graizer, 2007b, Extraction of near-surface properties for a lossy layered medium using the propagator matrix: Geophysical Journal International, **169**, 271–280.
——, 2007c, Down-hole receiver function: A case study: Bulletin of the Seismological Society of America, **97**, 1396–1403.
Ramirez, A. C., K. Hokstad, and E. Otnes, 2007a, Data driven regularization/extrapolation using interferometry: 69th Annual Conference and Exhibition, EAGE, Extended Abstracts, B032.
Ramirez, A. C., A. B. Weglein, E. Otnes, and K. Hokstad, 2007b, The role of the direct wave and Green's theorem in seismic interferometry and spurious multiples: 77th Annual International Meeting, SEG, Expanded Abstracts, 2473–2475.
Rickett, J. E., and J. F. Claerbout, 1999, Acoustic daylight imaging via spectral factorization: Helioseismology and reservoir monitoring: The Leading Edge, **19**, 957–960.
Riley, D. C., and J. F. Claerbout, 1976, 2-D multiple reflections: Geophysics, **41**, 592–620.
Rodberg, L. S., and R. M. Thaler, 1967, Introduction to the quantum theory of scattering: Academic Press, Inc.
Roux, P., W. A. Kuperman, and NPAL Group, 2004, Extracting coherent wave fronts from acoustic ambient noise in the ocean: Journal of the Acoustical Society of America, **116**, 1995–2003.
Sabra, K. G., P. Gerstoft, P. Roux, W. A. Kuperman, and M. Fehler, 2005a, Surface-wave tomography from microseisms in southern California: Geophysical Research Letters, **32**, L14311.
Sabra, K. G., P. Roux, and W. A. Kuperman, 2004, Arrival-time structure of the time-averaged ambient noise cross-correlation function in an oceanic waveguide: Journal of the Acoustical Society of America, **117**, 164–174.
Sabra, K. G., P. Roux, A. M. Thode, G. L. D'Spain, and W. S. Hodgkiss, 2005b, Using ocean ambient noise for array self-localization and self-synchronization: IEEE Journal of Oceanic Engineering, **30**, 338–347.
Sánchez-Sesma, F., and M. Campillo, 2006, Retrieval of the Green's function from cross correlation: The canonical elastic problem: Bulletin of the Seismological Society of America, **96**, 1182–1191.
Sava, P., and O. Poliannikov, 2008, Interferometric imaging condition for wave-equation migration: Geophysics, **73**, no. 2, S47–S61.
Schuster, G. T., F. Followill, L. J. Katz, J. Yu, and Z. Liu, 2004, Autocorrelogram migration: Theory: Geophysics, **68**, 1685–1694.
Shapiro, N. M., M. Campillo, L. Stehly, and M. H. Ritzwoller, 2005, High-resolution surface-wave tomography from ambient seismic noise: Science, **307**, 1615–1618.
Snieder, R., 2004, Extracting the Green's function from the correlation of coda waves: A derivation based on stationary phase: Physical Review E, **69**, 046610.

———, 2006, Retrieving the Green's function of the diffusion equation from the response to a random forcing: Physical Review E, **74**, 046620.

———, 2007, Extracting the Green's function of attenuating heterogeneous acoustic media from uncorrelated waves: Journal of the Acoustical Society of America, **121**, 2637–2643.

Snieder, R., and E. Şafak, 2006, Extracting the building response using seismic interferometry: Theory and application to the Millikan Library in Pasadena, California: Bulletin of the Seismological Society America, **96**, 586–598.

Snieder, R., J. Sheiman, and R. Calvert, 2006a, Equivalence of the virtual-source method and wave-field deconvolution in seismic interferometry: Physical Review E, **73**, 066620.

Snieder, R., K. Wapenaar, and K. Larner, 2006b, Spurious multiples in seismic interferometry of primaries: Geophysics, **71**, no. 4, SI111–SI124.

Snieder, R., K. Wapenaar, and U. Wegler, 2007, Unified Green's function retrieval by cross-correlation: Connection with energy principles: Physical Review E, **75**, 036103.

Stoffa, P. L., J. T. Fokkema, R. M. de Luna Freire, and W. P. Kessinger, 1990, Split-step Fourier migration: Geophysics, **55**, 410–421.

Trampert, J., M. Cara, and M. Frogneux, 1993, *SH* propagator matrix and Q_s estimates from borehole- and surface-recorded earthquake data: Geophysical Journal International, **112**, 290–299.

van Wijk, K., 2006, On estimating the impulse response between receivers in a controlled ultrasonic experiment: Geophysics, **71**, no. 4, SI79–SI84.

Vasconcelos, I., 2007, Inteferometry in perturbed media: Ph.D. dissertation, Colorado School of Mines.

Vasconcelos, I., and R. Snieder, 2008, Interferometry by deconvolution–Part 2: Theory for elastic waves and application to drill-bit seismic imaging: Geophysics, **73**, no. 3, S129–S141.

Vasconcelos, I., R. Snieder, and B. Hornby, 2007, Target-oriented interferometry — Imaging with internal multiples from subsalt VSP data: 77th Annual International Meeting, SEG, Expanded Abstracts, 3069–3073.

Vasconcelos, I., S. T. Taylor, R. Snieder, J. A. Chavarria, P. Sava, and P. Malin, 2007, Broadside interferometric and reverse-time imaging of the San Andreas fault at depth: 77th Annual International Meeting, SEG, Expanded Abstracts, 2175–2179.

Wapenaar, K., 2006, Green's function retrieval by cross-correlation in case of one-sided illumination: Geophysical Research Letters, **33**, L19304.

———, 2007, General representations for wavefield modeling and inversion in geophysics: Geophysics, **72**, no. 5, SM5–SM17.

Wapenaar, K., and J. Fokkema, 2006, Green's function representations for seismic interferometry: Geophysics, **71**, no. 4, SI33–SI46.

Wapenaar, K., E. Slob, and R. Snieder, 2006, Unified Green's function retrieval by cross correlation: Physical Review Letters, **97**, 234301.

Wapenaar, K., J. Thorbecke, and D. Draganov, 2004, Relations between reflection and transmission responses of three-dimensional inhomogeneous media: Geophysical Journal International, **156**, 179–194.

Weaver, R. L., and O. I. Lobkis, 2001, Ultrasonics without a source: Thermal fluctuation correlations and MHz frequencies: Physical Review Letters, **87**, 134301.

———, 2004, Diffuse fields in open systems and the emergence of the Green's function: Journal of the Acoustical Society of America, **116**, 2731–2734.

Weglein, A. B., F. V. Araújo, P. M. Carvalho, R. H. Stolt, K. H. Matson, R. T. Coates, D. Corrigan, D. J. Foster, S. A. Shaw, and H. Zhang, 2003, Inverse scattering series and seismic exploration: Inverse Problems, **19**, R27–R83.

Yu, J., and G. T. Schuster, 2006, Crosscorrelogram migration of inverse vertical seismic profile data: Geophysics, **71**, no. 1, S1–S11.